Rapid Communications | Editors' Suggestion

Revealing the hidden heavy Fermi liquid in $CaRuO_3$

Yang Liu,[1,2,3] Hari P. Nair,[3] Jacob P. Ruf,[2] Darrell G. Schlom,[3,4] and Kyle M. Shen[2,4,*]

[1]*Center for Correlated Matter and Department of Physics, Zhejiang University, Hangzhou 310058, China*

[2]*Laboratory of Atomic and Solid State Physics, Department of Physics, Cornell University, Ithaca, New York 14853, USA*

[3]*Department of Materials Science and Engineering, Cornell University, Ithaca, New York 14853, USA*

[4]*Kavli Institute at Cornell for Nanoscale Science, Ithaca, New York 14853, USA*

(Received 28 November 2017; revised manuscript received 10 May 2018; published 25 July 2018)

The perovskite ruthenate $CaRuO_3$ has attracted considerable interest due to reports of possible non-Fermi-liquid behavior and its proximity to a magnetic quantum critical point, yet its ground state and electronic structure remain enigmatic. Here, we report measurements of the Fermi surface and quasiparticle dispersion in $CaRuO_3$ through a combination of oxide molecular beam epitaxy and *in situ* angle-resolved photoemission spectroscopy. Our results reveal a complex and anisotropic Fermi surface consisting of small electron pockets and straight segments, consistent with the bulk orthorhombic crystal structure with large octahedral rotations. We observe a strongly band-dependent mass renormalization, with prominent heavy quasiparticle bands which lie close to the Fermi energy and exhibit a strong temperature dependence. These results are consistent with a heavy Fermi liquid with a complex fermiology and small hybridization gaps near the Fermi energy. Our results provide a unified framework for explaining previous experimental results on $CaRuO_3$, such as its unusual optical conductivity, and demonstrate the importance of octahedral rotations in determining the quasiparticle band structure, and electron correlations in complex transition-metal oxides.

DOI: 10.1103/PhysRevB.98.041110

The ruthenates host a remarkably diverse class of exotic quantum phases, ranging from spin-triplet superconductivity, ferromagnetism, metamagnetism, spin-density waves, and quantum criticality, all with the same basic building block of corner-sharing RuO_6 octahedra with a central Ru^{4+} ion [1–3]. Among the ruthenates, $CaRuO_3$ remains a particularly enigmatic compound. Measurements of the optical conductivity ($\sigma_1 \propto \omega^{-1/2}$) and resistivity [$\rho(T) \propto T^{3/2}$] have suggested that paramagnetic $CaRuO_3$ exhibits a non-Fermi-liquid (NFL) ground state [4–7], where the electronic excitations cannot be mapped directly to single-electron excitations, giving rise to physical properties not described by conventional Fermi-liquid (FL) theory. Indeed, given its close similarity to its isostructural and isoelectronic ferromagnetic counterpart, $SrRuO_3$, it has been argued that $CaRuO_3$ might be on the cusp of a magnetic quantum critical point [5,7,8], given the strong ferromagnetic fluctuations seen in nuclear magnetic resonance and induced ferromagnetism by defects and dopings [9–12]. On the other hand, the strong interplay between Hund's coupling J and electronic on-site repulsion U in $CaRuO_3$ could give rise to a fragile FL with a low coherence temperature, as recently proposed by dynamical mean-field theory (DMFT) [13–17] and supported by transport measurements below 2 K [18]. In particular, it has been proposed theoretically that the large RuO_6 octahedral rotations in $CaRuO_3$ may give rise to a multitude of low-lying interband transitions that could mimic NFL effects in the optical conductivity [15,19]. Nevertheless, precise knowledge of the momentum-dependent electronic structure, particularly the Fermi surface (FS), is crucial for understanding the true nature of the ground state and electromagnetic properties of $CaRuO_3$.

In this Rapid Communication, we report momentum-resolved measurements of quasiparticle (QP) dispersions and FS in $CaRuO_3$, by combining high-quality thin-film growth by reactive-oxide molecular-beam epitaxy (MBE) and *in situ* angle-resolved photoemission spectroscopy (ARPES) measurements. Our data reveal sharp, well-defined QP excitations that form a complex band structure arising from the large $GdFeO_3$-type distortions in $CaRuO_3$, confirming its FL ground state. We observe a manifold of heavy, flat QP bands close to the Fermi energy (E_F) caused by large octahedral rotations. Our measurement of the low-energy electronic structure provides a unified framework for explaining both the unconventional optical and terahertz conductivity [4,15,18,19] as arising from low-lying interband transitions, as well as the large electronic specific heat ($\sim$80 mJ/mol K^2) [7,20], and crossover behavior in resistivity and the Hall coefficient with temperature, originating from the unexpectedly heavy QP bands.

Epitaxial thin films of $CaRuO_3$, typically $\sim$20 nm, were grown by MBE in a dual-chamber Veeco GEN10 system in an oxidant ($\sim$90% O_2 + 10% O_3) background pressure of 8×10^{-7} Torr and a substrate temperature of 800 °C, as measured using the k-space BandiT detector operating in the blackbody mode. The film growth was monitored in real time using reflection high-energy electron diffraction (RHEED). Growth of (001)- and (110)-oriented $CaRuO_3$ films was achieved by selecting similarly oriented $NdGaO_3$ (NGO) substrates. Immediately after growth, thin films were transferred under ultrahigh vacuum to a high-resolution ARPES system consisting of a VG Scienta R4000 analyzer and a VUV5000 helium plasma

*Author to whom correspondence should be addressed: kmshen@cornell.edu

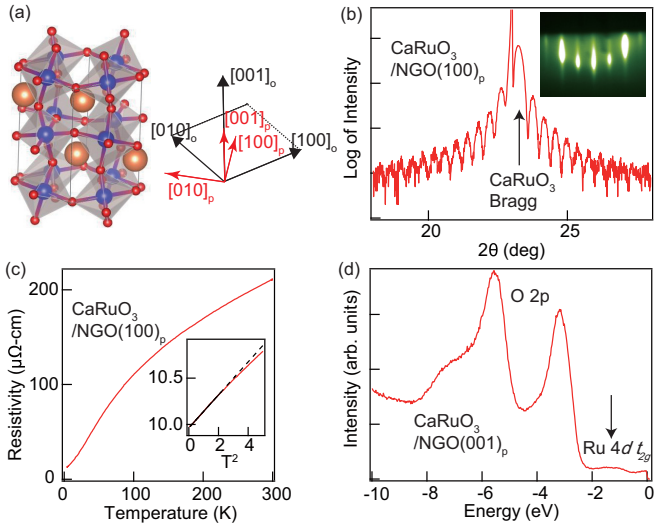

FIG. 1. (a) Crystal structure (the orthorhombic unit cell is indicated by black box) and correspondence between the orthorhombic (o) and pseudocubic (p) lattice. The brown, blue, and red spheres represent Ca, Ru, and O atoms, respectively. (b) *Ex situ* x-ray diffraction scan along the out-of-plane direction. The inset shows the RHEED pattern along the $\langle 001\rangle_p$ azimuth angle during the growth. (c) Resistivity as a function of temperature for the same ARPES sample shown in Figs. 2(d)–2(f). The inset is a ρ vs T^2 plot at very low temperature, highlighting a very low FL coherence temperature of ∼1.5 K, deduced by deviation from a simple T^2 fitting at low temperature (black dashed line). (d) Valence band photoemission along the surface normal direction for $CaRuO_3$ $(001)_p$ film.

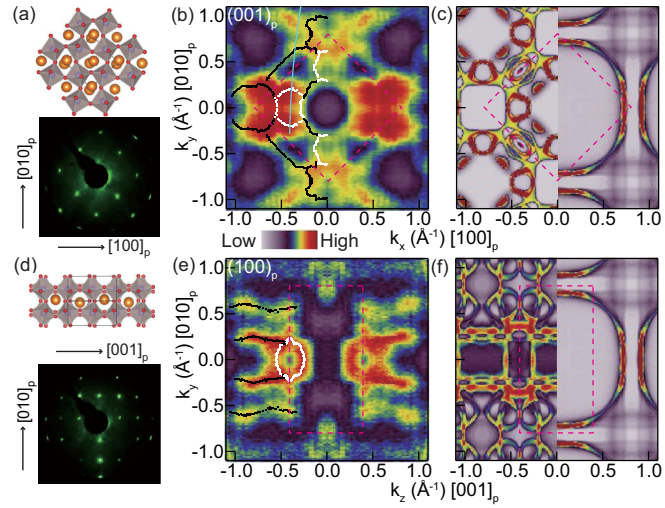

FIG. 2. (a) and (d) Top view of the crystal structure of (a) $(001)_p$ and (d) $(100)_p$ terminated surfaces, showing a $(\sqrt{2}\times\sqrt{2})R45^\circ$ and 2×2 LEED pattern in pseudocubic coordinates, respectively (taken at 66 eV). (b) and (e) are the experimentally measured FSs of $CaRuO_3$ (b) $(001)_p$ and (e) $(100)_p$ films, which are presented in image plots with the color scale shown in the middle (red indicates high intensity, light blue indicate low intensity). The purple dashed lines in (b), (c), (e), and (f) mark the projected bulk Brillouin zone (BZ) boundary. The extracted Fermi contours are displayed on the left half as black and white dots, for light and heavy QPs, respectively. The slanted cyan line in (b) shows the momentum cut position in Fig. 3. (c) and (f) are the simulated ARPES spectra from DFT calculations for (c) $(001)_p$ and (f) $(100)_p$ films, respectively. The left halves in (c) and (f) are simulations using a realistic orthorhombic structure, and the right halves are simulations assuming a cubic structure without octahedral rotation. The simulations of the FS maps use appropriate k_z to match the experimental data and assume a k_z broadening $(0.1\pi/a_0)$ and lifetime broadening (quadratic in energy expected for a FL), as described in detail in Ref. [25].

discharge lamp and monochromator [21]. Measurements were performed at 17 K (unless noted otherwise) with an energy resolution $\Delta E = 10$ meV with He Iα ($h\nu = 21.2$ eV) photons and a base pressure of 7×10^{-11} Torr. Spectra were also taken with He II ($h\nu = 40.81$ eV) photons to confirm the bulk nature of the observed bands shown in this work. After ARPES measurements, samples were characterized in detail by *in situ* low-energy electron diffraction (LEED), *ex situ* x-ray diffraction, electrical transport, and Hall measurements.

Figure 1(a) shows the crystal structure of bulk $CaRuO_3$ with its $a^-a^-c^+$-type octahedral rotations [22] which cause highly distorted RuO_6 octahedra and an orthorhombic lattice with lattice constants close to $(\sqrt{2}a_0, \sqrt{2}a_0, 2a_0)$, where a_0 is the pseudocubic lattice constant. Also shown in Fig. 1(a) is the correspondence between the orthorhombic (o) and pseudocubic (p) coordinate systems, which is commonly used to highlight the effect of octahedral rotations. The well-defined thickness fringes in x-ray diffraction [Fig. 1(b)] demonstrate the epitaxial, single-phase, and atomically flat nature of the thin films. In addition, RHEED [Fig. 1(b)] and low-energy electron diffraction [LEED, Figs. 2(a) and 2(d)] confirm that films with both the $(001)_o$ [same as $(001)_p$] and $(110)_o$ [same as $(100)_p$] out-of-plane orientations can be stabilized, which have subsequently been confirmed by *ex situ* transmission electron microscopy and synchrotron x-ray diffraction measurements. The typical residual resistivity ratios [RRR $= \rho(300\text{ K})/\rho(4\text{ K})$] of samples measured by ARPES are on the order of 20, and RRRs on other samples as high as 75 have been measured [23], indicating the high quality of the films. The resistivity exhibits a FL-like $\rho \propto T^2$ behavior below ∼1.5 K (hence a fragile FL), and a crossover to a $\rho \propto T^{1.5}$ behavior above 2 K, consistent with previous measurements [5–7,18,20]. Measurements of the valence band [Fig. 1(d)] show the O $2p$ and Ru $4d$ states, consistent with earlier reports by Yang *et al.* which focused on the origin of the broad hump around 1 eV binding energy (marked by an arrow) as being due to enhanced correlations [24].

In Fig. 2, we show maps in momentum space of the ARPES intensity at $E_F \pm 10$ meV, for films aligned both along the $(001)_p$ [Fig. 2(b)] and $(100)_p$ [Fig. 2(e)] directions. Both orientations show a complex FS comprising small pockets arising from the large $GdFeO_3$-type distortions, which cause band folding and hence small hole or electron pockets. The experimental Fermi wave vectors (k_Fs) from maxima in either the momentum distribution curves (MDCs) or energy distribution curves (EDCs) are summarized in the left halves in Figs. 2(b) and 2(e) as black dots. For the $(001)_p$ films, the experimental FS exhibits small pockets centered at (0,0), $(\pi/2, 0)$, and $(\pi, 0)$, and possibly $(\pi/2, \pi/2)$ (all defined within the pseudocubic coordinate). In comparison, we also

plot DFT simulations of the corresponding k-space maps calculated using WIEN2K in the generalized gradient approximation (details in Supplemental Material [25]) in Figs. 2(c) and 2(f): the left for the bulk structure (structure parameters adapted from Ref. [26]), and the right for the ideal cubic structure with 180° Ru-O-Ru bonds. By comparing the experimental data with various k_z slices through the DFT calculation, we estimate $k_z \sim 0.5\pi/a_0$ for the $(001)_p$ surface and $k_z \sim 0.7\pi/a_0$ for the $(100)_p$ surface under $h\nu = 21.2$ eV photons (Figs. S1 and S2 in Ref. [25]). Those values of k_z suggest an inner potential of 14.4 ± 2 and 11 ± 2 eV for the $(001)_p$ and $(100)_p$ surfaces, respectively, similar to $SrRuO_3$ [27]. The orthorhombic DFT calculations in the left half of Fig. 2(c) qualitatively reproduce the multiplicity of small FS pockets, in contrast to the case of $SrRuO_3$, where the band folding is much weaker [28–31]. Despite sharing the same $Pbnm$ structure, the rotation angles of the oxygen octahedra are approximately doubled in $CaRuO_3$ compared to $SrRuO_3$ (the averaged rotation angle along each of the three pseudocubic axes is ∼5° in $SrRuO_3$ versus ∼11° for $CaRuO_3$ [32,33]). This leads to a significant difference in the momentum distribution of spectral weight, from reflecting nearly cubic symmetry in $SrRuO_3$, to a much more complex structure in $CaRuO_3$, and could be important for the observed differences in electromagnetic properties (Table I in Ref. [25]).

The importance of octahedral rotations is even more evident when comparing the $(001)_p$ data to that from the $(100)_p$ surface, which should be identical in the idealized cubic structure without rotations [right halves in Figs. 2(c) and 2(f)]. The ARPES Fermi-surface maps show dramatic differences [Fig. 2(e)] between the two orientations. For instance, in the $(100)_p$ films, there is only a single enclosed pocket near $(\pi/2, 0)$, together with long straight segments of high intensity running parallel to the $[001]_p$ direction which qualitatively match the corresponding orthorhombic DFT simulations for this surface. The average radius of this electron pocket is measured to be 0.15 $Å^{-1}$, which is in agreement with the only frequency seen from Shubnikov–de Haas (SdH) oscillations (0.12 $Å^{-1}$) in similarly oriented $(100)_p$ films [18]. SdH oscillation results from an $(001)_p$ film are not available at the moment, but additional frequencies have been observed as the magnetic field is moved from $[100]_p$ towards the $[001]_p$ direction [18], which is consistent with the ARPES FS map of $(001)_p$ films, showing additional small pockets due to strong band folding.

In Fig. 3(a), we show the EDCs along the momentum cut shown by the cyan line in Fig. 2(b). A weakly dispersive, sharp QP peak is clearly observed close to E_F and whose intensity is highly dependent on the RRR, underscoring the importance of sample quality. The image plot is shown in Fig. 3(b), which also reveals a neighboring, broader band with significant dispersion (effective mass $0.8m_e$). To accurately extract the heavy QP dispersion, we divide the measured ARPES spectra by the Fermi-Dirac function convolved by a Gaussian resolution function [25]. The results reveal that the heavy QP band is electronlike with a fitted effective mass $m^* = 13.5 \pm 1.5m_e$ [black dots in Fig. 3(b)]. The experimental data on $(100)_p$ films further confirm that these heavy QPs possess large masses along all three momentum directions (Fig. S4 in Ref. [25]), which allow us to calculate the electronic

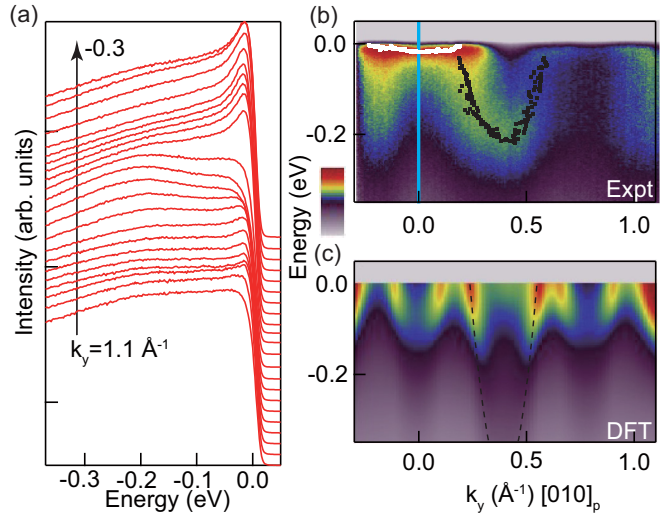

FIG. 3. (a) Waterfall and (b) image plot of energy-momentum cuts for $(001)_p$-oriented films. The cut is along the slanted cyan line shown in Fig. 2(b). The experimentally extracted QP dispersion is shown as white (black) dots, for heavy (light) QP bands, respectively. The heavy QP dispersion near E_F is extracted from Fig. S5 in Ref. [25]. (c) shows simulated ARPES spectra based on DFT calculations, along the same momentum cut as (b). Black dashed curves indicate DFT calculated light QP dispersion. Appropriate energy and k_z broadening have been taken into account for the simulation [25].

specific heat associated with these heavy QPs to be 60 ± 6.7 mJ/mol K^2 [25], accounting for a large portion of the experimental specific heat (∼80 mJ/mol K^2). The remainder could be due to contributions from other lighter bands. DFT calculations for the bulk-like structure predicts $m^* \sim 1m_e$ for all relevant bands [see Fig. 3(c)] [25]. This strongly band-dependent renormalization, and the subsequent coexistence of heavy and light QPs near E_F, is remarkable, and the origin of such large variations in the renormalization of bands from presumably the same orbitals remains unclear. As a result, only the light QP bands measured in the experiment agree well with the DFT simulations of the Fermi surface and band dispersion [Figs. 2(c), 2(f) and 3(c)], while the heavy QP bands show strong discrepancies with the DFT calculations due to their much stronger renormalization (the heavy bands were not used in comparing the Fermi-surface topologies or k_z determination for this reason). This strongly band-dependent renormalization and major discrepancies for the heavy bands indicate that DFT alone cannot explain the QP dispersion in $CaRuO_3$, and the inclusion of on-site Hubbard repulsion and Hund's coupling is likely essential. A full description of the electronic structure requires advanced theoretical tools, such as DFT+DMFT [13,16,17].

We emphasize that the observed QP bands are most likely derived from bulk, rather than surface states, given the clear differences in data taken with different photon energies (Fig. S6 in Ref. [25]). Moreover, the heat capacity estimated from ARPES measurements matches closely to the bulk thermodynamic measurements, suggesting that the heavy QP bands which dominate this calculation probably correspond to bulk electronic states. In addition, the light QP bands are in qualitative agreement with bulk DFT calculations. While it

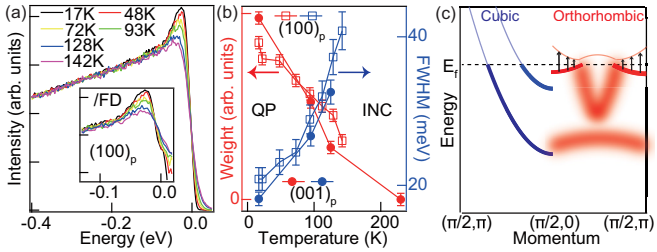

FIG. 4. (a) Temperature dependence of heavy QP band for $(100)_p$ film at the $(\pi/2, 0)$ pocket [white vertical cut in Fig. S4(b) in Ref. [25]]. The inset is the EDCs divided by the Fermi-Dirac function convoluted by a Gaussian function, revealing the full spectral function above E_F. (b) Deduced QP spectral weight (red symbols, left axis) and full width at half maximum (FWHM, blue symbols, right axis), which is proportional to the QP scattering rate. Data from both a $(001)_p$ film (solid circle) and a $(100)_p$ film (open rectangular) are shown. The charge carriers exhibit a gradual crossover from well-defined QP at low temperature to incoherent (INC) carrier at high temperature. The raw data for the $(001)_p$ film are included in Fig. S5(b) in Ref. [25]. (c) Cartoon showing the origin and implication of heavy QP in $CaRuO_3$. The horizontal (vertical) axis is the momentum (energy). The left half illustrates the QP spectra for the cubic phase without rotation, and the right half shows the case after considering rotation.

is difficult to conclusively rule out subtle surface relaxations, the combination of the photon energy dependence and the agreement with bulk measurements and calculations, when taken as a whole, suggests that any possible surface relaxation is minimal enough not to qualitatively affect our observations, as supported by the LEED measurements which are also consistent with the bulk symmetry (Fig. 2).

A central question for $CaRuO_3$ remains the robustness of the FL ground state, given the apparently low FL coherence temperature (1.5 K) deduced from resistivity measurements [Fig. 1(c)]. We perform temperature-dependent ARPES measurements and in fact observe well-defined QP peaks up to 100 K [Fig. 4(a)], thus providing direct spectroscopic evidence of robust FL-like QPs even to high temperatures. A detailed line-shape analysis shows the disappearance of the heavy QPs at ∼150 K in Fig. 4(b), corresponding to the crossover in resistivity [Fig. 1(c)] and rapid change of Hall coefficient [25,34]. Such a temperature dependence has also been reported in other ruthenates [35,36] and has been proposed to be a direct signature of strong correlations in a Hund's metal [14], where the interplay between U and J results in a large intermediate temperature range where the coherent spectral weight shows a strong temperature dependence [16,37,38]. The observation of heavy QPs with a strong temperature dependence, together with the large electronic specific heat and crossover behavior in the resistivity and Hall coefficient, indicate a heavy Fermi-liquid ground state with surprising similarities to heavy fermion systems [39]. Whether there is any inherent connection between two systems would be an interesting topic of investigation for future studies.

In Fig. 4(c), we show a schematic summarizing our key observations for $CaRuO_3$, where large octahedral rotations cause strong band folding and hybridization, resulting in a complex Fermi-surface topology with many small electron or hole pockets and hybridization gaps near E_F. Our results allow for a unified understanding of not only its electronic structure, but also the myriad experimental observations previously reported in the literature. The complex band structure, comprising many heavy bands which lie within 30 meV (7.25 THz or 242 cm^{-1}) of E_F, is the origin of the multitude of low-energy interband transitions, which mimics the signature of NFL optical conductivity previously reported. The large rotations also significantly reduce the bandwidth, leading to large mass renormalization for some bands near E_F, while other light QPs coexist. This strongly band-dependent mass renormalization is remarkable and its origin is yet to be understood theoretically. The heavy QPs exhibit a strong temperature dependence, a signature of strong correlation in Hund's metals. Our results not only provide an experimental understanding of the complex electronic structure of $CaRuO_3$, but generally highlight the importance of octahedral rotations in correlated ruthenate perovskites and how they can impact the fermiology and physical properties in a much more pronounced manner than other prototypical metallic perovskites, e.g., $SrVO_3/CaVO_3$ [40].

We would like to thank A. Georges, Q. Han, and A. J. Millis for very helpful discussions and insights. This work was supported by the National Science Foundation through DMR-1709255, DMR-1308089, and through the Materials Research Science and Engineering Centers program (DMR-1719875, the Cornell Center for Materials Research), and the Research Corporation for Science Advancement (2002S). This work was performed in part at the Cornell NanoScale Facility, a member of the National Nanotechnology Infrastructure Network, which is supported by the National Science Foundation (Grant No. ECCS-0335765). Y.L. acknowledges support from National Natural Science Foundation of China (Grant No. 11674280) and National Key R&D program of the MOST of China (Grant No. 2016YFA0300203).

Y.L. and H.P.N. contributed equally to this work.

[1] A. P. Mackenzie and Y. Maeno, Rev. Mod. Phys. **75**, 657 (2003).

[2] S. A. Grigera, R. S. Perry, A. J. Schofield, M. Chiao, S. R. Julian, G. G. Lonzarich, S. I. Ikeda, Y. Maeno, A. J. Millis, and A. P. Mackenzie, Science **294**, 329 (2001).

[3] G. Koster, L. Klein, W. Siemons, G. Rijnders, J. S. Dodge, C.-B. Eom, D. H. A. Blank, and M. R. Beasley, Rev. Mod. Phys. **84**, 253 (2012).

[4] Y. S. Lee, J. Yu, J. S. Lee, T. W. Noh, T.-H. Gimm, H.-Y. Choi, and C. B. Eom, Phys. Rev. B **66**, 041104 (2002).

[5] L. Klein, L. Antognazza, T. H. Geballe, M. R. Beasley, and A. Kapitulnik, Phys. Rev. B **60**, 1448 (1999).

[6] L. Capogna, A. P. Mackenzie, R. S. Perry, S. A. Grigera, L. M. Galvin, P. Raychaudhuri, A. J. Schofield, C. S. Alexander, G. Cao, S. R. Julian, and Y. Maeno, Phys. Rev. Lett. **88**, 076602 (2002).

[7] G. Cao, O. Korneta, S. Chikara, L. E. DeLong, and P. Schlottmann, Solid State Commun. **148**, 305 (2008).
[8] I. I. Mazin and D. J. Singh, Phys. Rev. B **56**, 2556 (1997).
[9] K. Yoshimura, T. Imai, T. Kiyama, K. R. Thurber, A. W. Hunt, and K. Kosuge, Phys. Rev. Lett. **83**, 4397 (1999).
[10] T. He and R. J. Cava, Phys. Rev. B **63**, 172403 (2001).
[11] A. Maignan, B. Raveau, V. Hardy, N. Barrier, and R. Retoux, Phys. Rev. B **74**, 024410 (2006).
[12] V. Durairaj, S. Chikara, X. N. Lin, A. Douglass, G. Cao, P. Schlottmann, E. S. Choi, and R. P. Guertin, Phys. Rev. B **73**, 214414 (2006).
[13] A. Georges, L. de'Medici, and J. Mravlje, Annu. Rev. Condens. Matter Phys. **4**, 137 (2013).
[14] J. Mravlje, M. Aichhorn, T. Miyake, K. Haule, G. Kotliar, and A. Georges, Phys. Rev. Lett. **106**, 096401 (2011).
[15] H. T. Dang, J. Mravlje, A. Georges, and A. J. Millis, Phys. Rev. Lett. **115**, 107003 (2015).
[16] H. T. Dang, J. Mravlje, A. Georges, and A. J. Millis, Phys. Rev. B **91**, 195149 (2015).
[17] X. Deng, K. Haule, and G. Kotliar, Phys. Rev. Lett **116**, 256401 (2016).
[18] M. Schneider, D. Geiger, S. Esser, U. S. Pracht, C. Stingl, Y. Tokiwa, V. Moshnyaga, I. Sheikin, J. Mravlje, M. Scheffler, and P. Gegenwart, Phys. Rev. Lett. **112**, 206403 (2014).
[19] D. Geiger, U. S. Pracht, M. Dressel, J. Mravlje, M. Schneider, P. Gegenwart, and M. Scheffler, Phys. Rev. B **93**, 165131 (2016).
[20] N. Kikugawa, L. Balicas, and A. P. Mackenzie, J. Phys. Soc. Jpn. **78**, 014701 (2009).
[21] E. J. Monkman, C. Adamo, J. A. Mundy, D. E. Shai, J. W. Harter, D. Shen, B. Burganov, D. A. Muller, D. G. Schlom, and K. M. Shen, Nat. Mater. **11**, 855 (2012).
[22] A. M. Glazer, Acta Crystallogr., Sect. B **28**, 3384 (1972).
[23] H. P. Nair, Y. Liu, J. P. Ruf, N. J. Schreiber, S.-L. Shang, D. J. Baek, B. H. Goodge, L. F. Kourkoutis, Z.-K. Liu, K. M. Shen, and D. G. Schlom, APL Mater. **6**, 046101 (2018).
[24] H. F. Yang, C. C. Fan, Z. T. Liu, Q. Yao, M. Y. Li, J. S. Liu, M. H. Jiang, and D. W. Shen, Phys. Rev. B **94**, 115151 (2016).
[25] See Supplemental Material at http://link.aps.org/supplemental/10.1103/PhysRevB.98.041110 for detailed discussions.
[26] A. T. Zayak, X. Huang, J. B. Neaton, and K. M. Rabe, Phys. Rev. B **74**, 094104 (2006).
[27] M. Takizawa, Ph.D. thesis, University of Tokyo, 2007.
[28] A. P. Mackenzie, J. W. Reiner, A. W. Tyler, L. M. Galvin, S. R. Julian, M. R. Beasley, T. H. Geballe, and A. Kapitulnik, Phys. Rev. B **58**, R13318 (1998).
[29] C. S. Alexander, S. McCall, P. Schlottmann, J. E. Crow, and G. Cao, Phys. Rev. B **72**, 024415 (2005).
[30] D. E. Shai, C. Adamo, D. W. Shen, C. M. Brooks, J. W. Harter, E. J. Monkman, B. Burganov, D. G. Schlom, and K. M. Shen, Phys. Rev. Lett. **110**, 087004 (2013).
[31] H. F. Yang, Z. T. Liu, C. C. Fan, Q. Yao, P. Xiang, K. L. Zhang, M. Y. Li, H. Li, J. S. Liu, D. W. Shen, and M. H. Jiang, Phys. Rev. B **93**, 121102 (2016).
[32] J.-G. Cheng, J.-S. Zhou, and John B. Goodenough, Proc. Natl. Acad. Sci. U.S.A. **110**, 13312 (2013).
[33] T. Kiyama, K. Yoshimura, K. Kosuge, Y. Ikeda, and Y. Bando, Phys. Rev. B **54**, R756 (1996).
[34] S. C. Gausepohl, M. Lee, R. A. Rao, and C. B. Eom, Phys. Rev. B **54**, 8996 (1996).
[35] A. Shimoyamada, K. Ishizaka, S. Tsuda, S. Nakatsuji, Y. Maeno, and S. Shin, Phys. Rev. Lett. **102**, 086401 (2009).
[36] T. Kondo, M. Ochi, M. Nakayama, H. Taniguchi, S. Akebi, K. Kuroda, M. Arita, S. Sakai, H. Namatame, M. Taniguchi, Y. Maeno, R. Arita, and S. Shin, Phys. Rev. Lett. **117**, 247001 (2016).
[37] W. Xu, K. Haule, and G. Kotliar, Phys. Rev. Lett. **111**, 036401 (2013).
[38] X. Deng, J. Mravlje, R. Zitko, M. Ferrero, G. Kotliar, and A. Georges, Phys. Rev. Lett. **110**, 086401 (2013).
[39] F. Steglich, J. Aarts, C. D. Bredl, W. Lieke, D. Meschede, W. Franz, and H. Schafer, Phys. Rev. Lett. **43**, 1892 (1979).
[40] T. Yoshida, M. Hashimoto, T. Takizawa, A. Fujimori, M. Kubota, K. Ono, and H. Eisaki, Phys. Rev. B **82**, 085119 (2010).

Supplementary Materials for "Revealing the Hidden Heavy Fermi Liquid in $CaRuO_3$"

Yang Liu,[1,2,3] Hari P. Nair,[3] Jacob P. Ruf,[2] Darrell G. Schlom,[3,4] and Kyle M. Shen[2,4,*]

[1] *Center for Correlated Matter and Department of Physics, Zhejiang University, China*
[2] *Laboratory of Atomic and Solid State Physics, Department of Physics, Cornell University, Ithaca, New York 14853, USA*
[3] *Department of Materials Science and Engineering, Cornell University, Ithaca, New York 14853, USA*
[4] *Kavli Institute at Cornell for Nanoscale Science, Ithaca, New York 14853, USA*

In this supplementary document, we first present an estimate of specific heat based on our experimental electronic structure for $CaRuO_3$. A detailed comparison of physical properties between $CaRuO_3$ and $SrRuO_3$, based on relevant literatures and our current $CaRuO_3$ results, is summarized in Table I. We also present results from DFT band structure calculations (in Fig. S1-S3), and additional ARPES data (in Fig. S4-S6).

First let us calculate the electronic specific heat for $CaRuO_3$ based on our ARPES data and compare them with experimental specific heat. The electronic specific heat can be written as

$$\frac{C_v}{T} = \sum_i \frac{k_B^2 m_i k_{Fi} a_0^3 N_A}{3\hbar^2},$$

where k_B, N_A, $\hbar$ are the Boltzman, Avogadro, and Planck constants, m_i and k_{Fi} are the effective mass and Fermi wave vector for band i, and a_0 is the pseudocubic lattice constant for $CaRuO_3$ (3.85 Å). The summation is carried out for all valence bands (crossing Fermi level) within the first Brillouin zone of the pseudocubic lattice. Since the heavy QP lies near eight symmetry-similar points, $(k_x,\ k_y,\ k_z)=(\pm\pi/2, 0, \pm\pi/2)$ and $(k_x,\ k_y,\ k_z)=(0, \pm\pi/2, \pm\pi/2)$, with spin degeneracy of two, the summation yields a prefactor of 16. Using the experimental effective mass and Fermi wave vector (see Table I below), one obtains a contribution of 60 mJ / mol K^2 to the electronic specific heat from the heavy QP bands. A similar calculation has also been carried out for other lighter bands observed in ARPES. The total specific heat from all the observed light QP bands is estimated to be $\sim$ 10 mJ / mol K^2, which is much smaller than those from heavy QP bands, due to small effective mass. In general, the estimated specific heat from ARPES measurement ($\sim$ 70 mJ / mol K^2) is in reasonable agreement with experimental values ($\sim$ 80 mJ / mol K^2), highlighting the importance of the heavy QPs in shaping the thermodynamic properties of $CaRuO_3$.

Physical Properties	$SrRuO_3$	$CaRuO_3$
Octahedral Rotation	$\sim 5°$ [1]*	$\sim 11°$ [1]*
Resistivity	$\rho \propto T^2 < 40$ K [2]	$\rho \propto T^{1.5} > 2$ K $\rho \propto T^2 < 1.5$ K [3]
Specific heat	30 mJ / mol K^2 [4]	80 mJ / mol K^2 [5]
Magnetism	Ferromagnetic < 160 K	Paramagnetic
Fermiology	Mainly cubic Large pockets	Orthorhombic Small pockets
Fermi wave vector k_F	0.5 and 0.28 $Å^{-1}$ by ARPES [2], dHvA, SdH [6][7]	0.15 $Å^{-1}$ by ARPES** 0.12 $Å^{-1}$ by SdH [3]***
Effective mass	$\sim 3m_e$ by C_V [4] $4-6m_e$ by dHvA, SdH [6][7] $4m_e$ by ARPES [2]	$\sim 8m_e$ by C_V [5] $\sim 6m_e$ by SdH [3]*** ~ 0.8 to 14 m_e by ARPES

TABLE I. Comparison of physical properties between $SrRuO_3$ and $CaRuO_3$. dHvA and SdH are abbreviations for de Haas-van Alphen (dHvA) and Shubnikov-de Haas (SdH) measurements, respectively. *Here the rotation angle refers to the averaged rotation angle along each of the three pseudocubic axis, defined by Glazer's notation. **Only the ARPES results from $(110)_0$ (same as $(100)_p$) films are shown here for comparison with SdH results. ***SdH results are only reported for $(110)_0$ films at $<$ 1 K under large magnetic field. Based on Kadowaki-Woods relation, effective mass of $\sim 6m_e$ can be inferred at zero magnetic field at very low temperature.

Table I shows a compilation of related physical properties for $CaRuO_3$ and $SrRuO_3$. Being both isostructural ($Pbnm$) and isovalent (Ru^{4+}), the large difference of their electronic and magnetic properties could be attributed to the differing size of A-site cation and the resulting change in rotation of the RuO_6 octahedra.

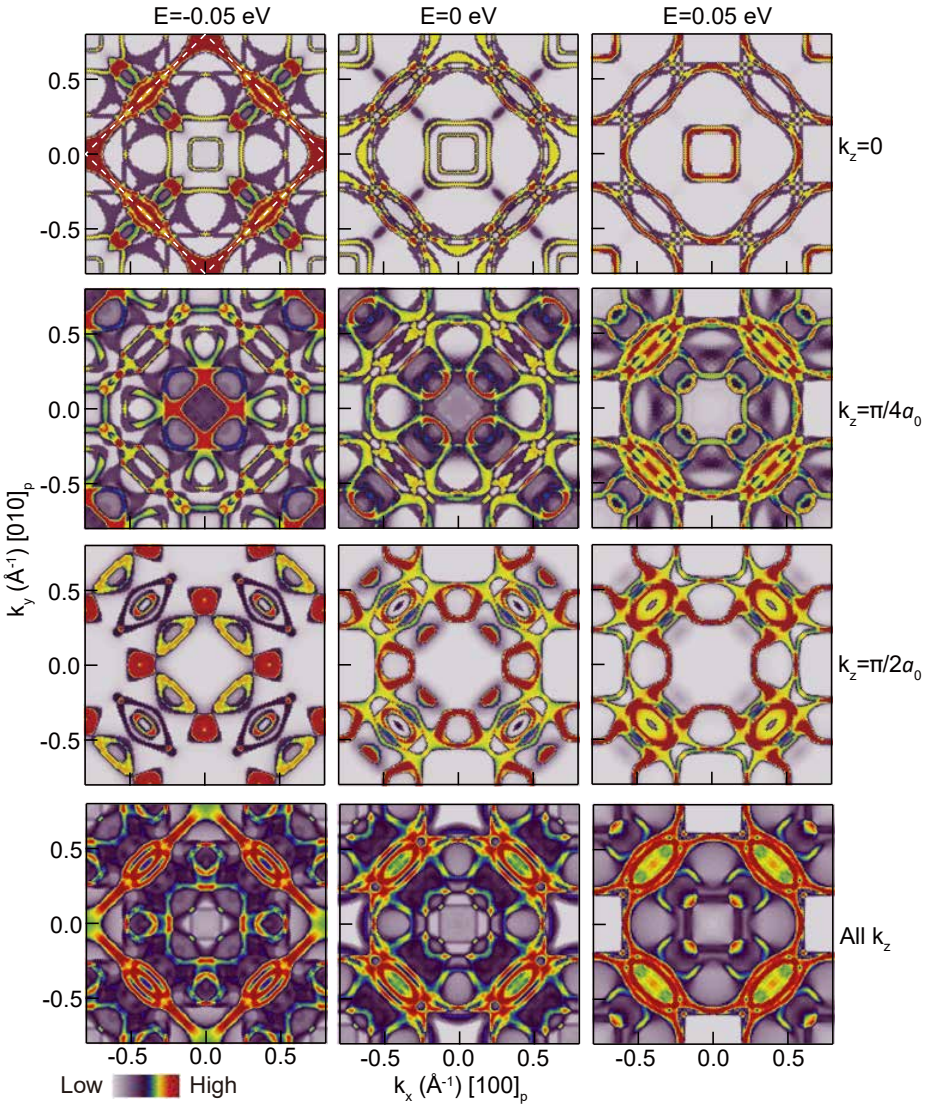

FIG. S 1. DFT simulated constant energy maps for a $(001)_p$ $CaRuO_3$ film at different energies (left to right) and k_z (top to bottom) cuts, to be compared with Fig. 2(b) in the manuscript. The bottom panels are simulated maps by integrating all k_z's (mimicking the experimental case where a very large k_z broadening occurs). The white dashed lines in the top left panel show the Brillouin zone boundary. Note that here k_z is defined in the pseudocubic lattice with lattice constant a_0, so $k_z = \pi/2a_0$ corresponds to the Brillouin zone boundary of the real orthorhombic lattice. These DFT simulations utilizes the band structure output from WIEN2k package and assumes appropriate momentum and energy broadening to yield the spectral function that can be directly compared with ARPES spectra. Specifically, the simulations at specific k_z cuts assume a fixed k_z broadening ($0.1\pi/a_0$, to take into account of limited escape depth of photoelectrons) and a QP lifetime broadening that is quadratic in energy as expected for a Fermi liquid, in order to match experimental results. For the bottom panels, an integration over all k_z's is performed to yield the simulated spectral function. We also assume a constant photoexcitation probability (matrix element), which is difficult to calculate directly and could be different from real experiments. The best match with the experimental FS is achieved at $E = 0\ eV$ and $k_z \sim \pi/2a_0$.

Fig. S1 shows the DFT simulated constant energy maps for $(001)_p$ film, which agree qualitatively with the experimental results when $E = 0\ eV$ and $k_z \sim \pi/2a_0$ (Fig. 2(b,c)). Both calculations and experiments show multiple small pockets as a result of strong band folding and mixing from oxygen octahedral rotation.

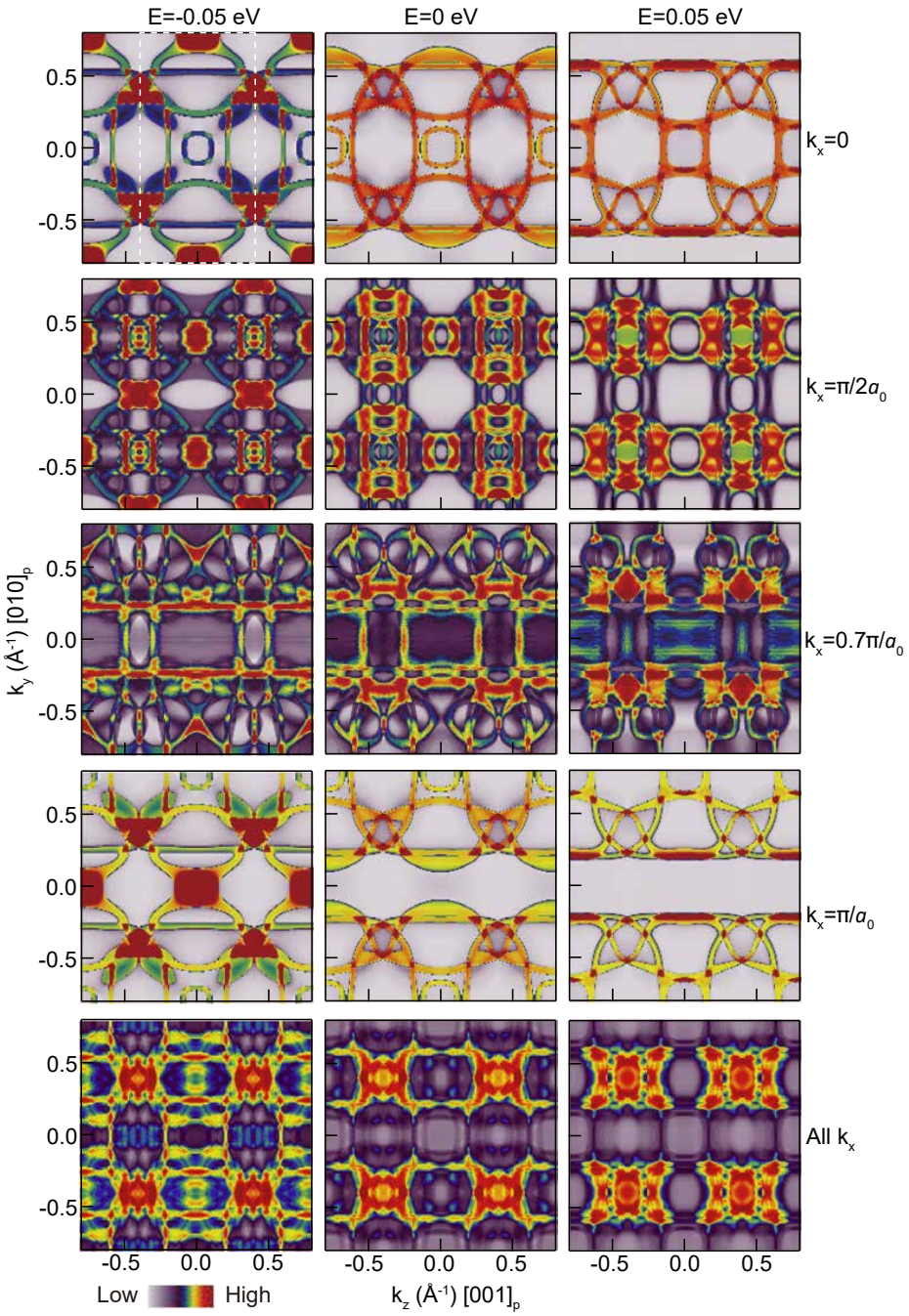

FIG. S 2. (a) DFT simulated constant energy maps for a $(100)_p$ $CaRuO_3$ film at different energies (left to right) and k_x (top to bottom) cuts, to be compared with Fig. 2(e) in the manuscript. The simulation is carried out in a similar manner as that of the $(001)_p$ film shown in Fig. S1. Note that for the $(100)_p$ film, the out-of-plane direction is along the pseudocubic k_x axis and the in-plane axis are along k_y and k_z, where very anisotropic band dispersion takes place due to oxygen octahedral rotation.

Figure S2 shows the DFT simulated constant energy maps for a $(100)_p$ $CaRuO_3$ film, which show very complex Fermiology with small pockets and many straight segments running along the k_z direction. While qualitative agreement between calculation and experiment can be found at $E = 0\ eV$ and $k_x \sim 0.7\ \pi/a_0$ (Fig. 2(e,f)), the quantitative agreement is not very good, likely due to inaccuracy in the DFT calculations as discussed in the manuscript.

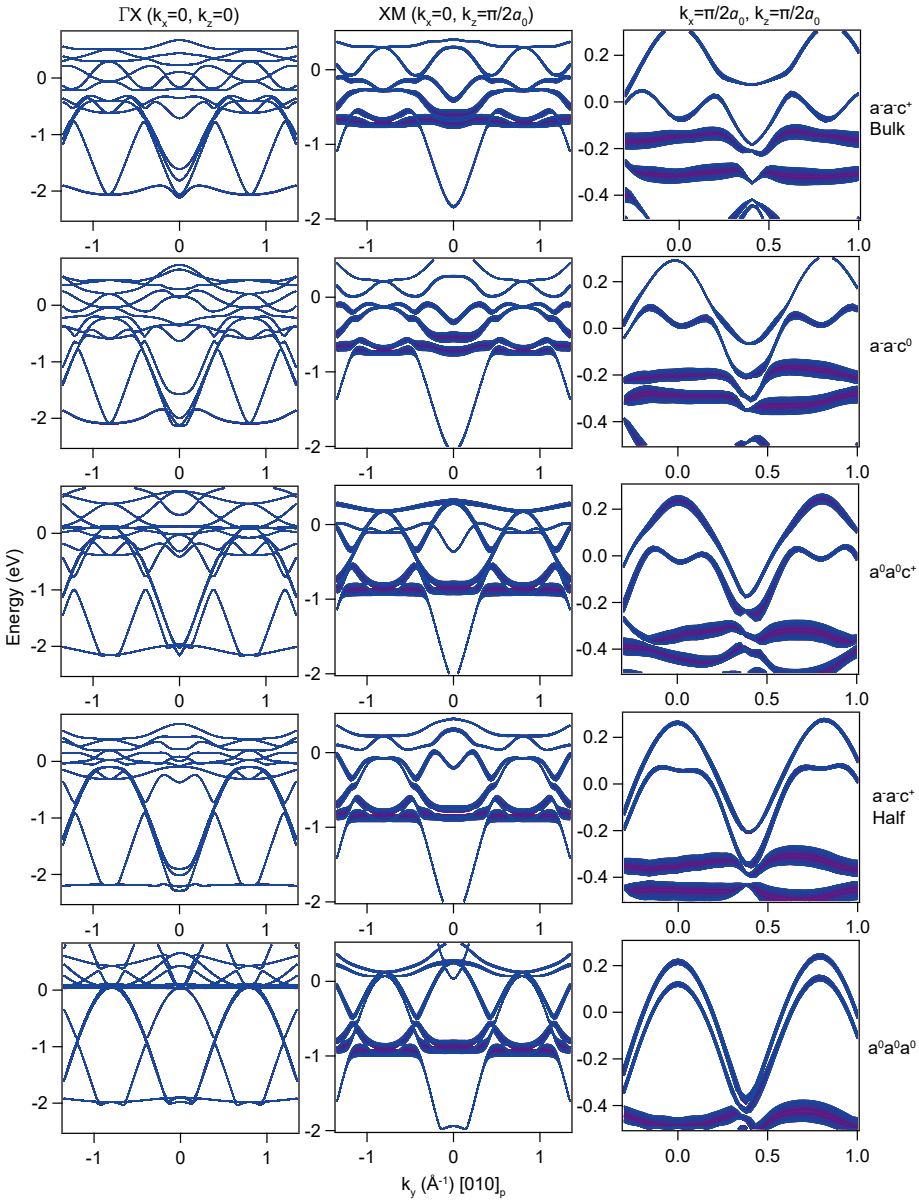

FIG. S 3. DFT band structure for $CaRuO_3$ with different octahedral rotations: from top to bottom rows shows results for bulk-like $a^-a^-c^+$ rotation, $a^-a^-c^0$ without z rotation, $a^0a^0c^+$ without x and y rotation, $a^-a^-c^+$ with half of the bulk rotation, and $a^0a^0c^0$ with no rotation, respectively. From left to right, columns are the dispersion relations along three different momentum cuts, as indicated on the top of the column. The rightmost column is at the same momentum cut as the experimental data in Figs. 3 and S5. The bulk lattice is adapted from [8]. Our DFT results for bulk-like $CaRuO_3$ is consistent with previous calculations [3][9]. Note that all labels refer to the pseudocubic lattice. The calculations includes a k_z broadening ($0.1\ \pi/a_0$) for comparison with ARPES data. Here all bands are plotted using the same color (blue) and the thickness of the bands indicate the energy spread after considering the k_z broadening, i.e., from k_z-0.1 to k_z+0.1.

Figure S3 shows the calculated band structure from DFT for different octahedral rotations. With increasing rotations, the band width decreases accordingly, which can be seen clearly for band dispersion plots along ΓX and XM. On the other hand, the effective mass near the Fermi level does not show significant increase with increasing rotation, e.g., the effective mass for bulk-like rotation is $\sim 0.8-1m_e$ along all three momentum directions in Fig. S3, which only shows marginal increase compared to the results for no rotations ($\sim 0.7m_e$). Detailed DFT calculations show that the momentum averaged effective mass for bulk-like rotation is only $\sim 1m_e$ [3], which is significantly lower than the value expected from specific heat measurement ($\sim 8m_e$). This indicates that while DFT can explain the

overall shape of the band structure, it does not provide a good quantitative description. In addition, DFT calculations do not reproduce any heavy QP band that exhibit similarly flat dispersion along all three momentum directions, as observed experimentally (Figs. 3(b) and S4(b)). For example, for $a^-a^-c^+$ with half of bulk rotation, DFT predicts a flat band above the Fermi level at (k_x, k_z)=($\pi/2, \pi/2$) cut (fourth row third column, same momentum cut as Fig. 3(b)), but it does not show similarly flat dispersion along the XM direction (fourth row second column), contrary to experimental results. Furthermore, the change of octahedral rotation (compared to the bulk case) is likey small due to the small lattice mismatch between $CaRuO_3$ films and $NdGaO_3$ substrates ($\sim 0.5\%$). Therefore, we conclude that the observed heavy QPs cannot be explained by pure lattice distortion within the DFT framework. An accurate description of electronic correlation, which is missing in DFT calculations, is essential to explain the heavy QP bands.

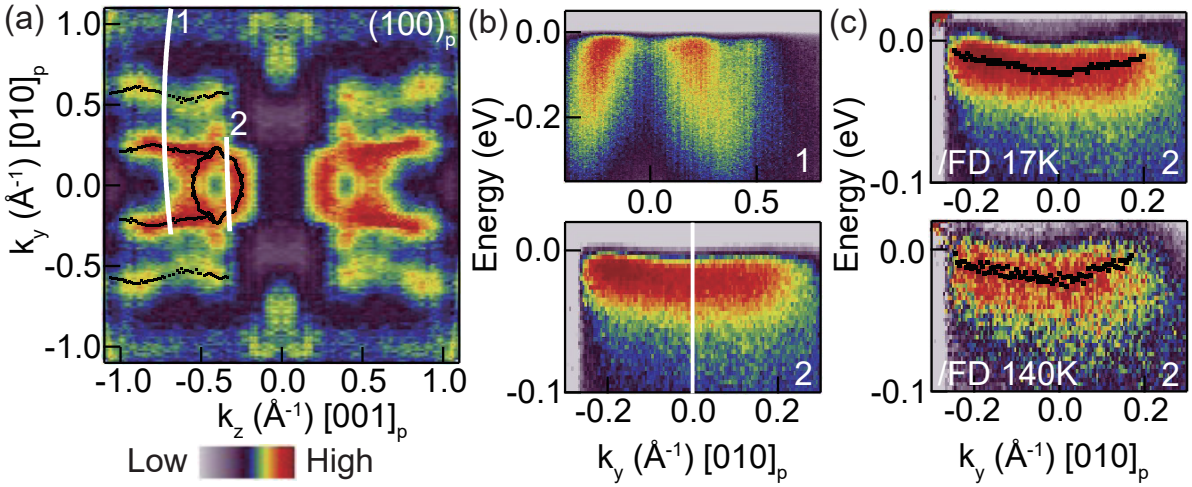

FIG. S 4. Energy-momentum cuts for $(100)_p$ oriented $CaRuO_3$ films. (a) Same data as Fig. 2(e), with the slanted white curves showing the momentum cut positions in (b,c). (b) the energy-momentum cuts taken at 17 K, showing the light QP (top) and heavy QP (bottom) bands at different momentum positions. (c) energy-momentum cut 2 divided by the Fermi-Dirac function convoluted with a Gaussian function, at 17 K (top) and 140 K (bottom), respectively, showing the full spectral function near the Fermi level at two representative temperatures. The black dots are extracted QP positions from EDCs.

In Fig. S4, we show additional ARPES data and analysis from $(100)_p$ oriented films. In contrast to the $(001)_p$ oriented film (Fig. 2(b)), the FS shows only one type of enclosed pockets centered at $(k_y,k_z)=(0,\pm\pi/2)$, and parallel segments running along the $[001]_p$ direction. Energy-momentum cuts reveal that the straight segments possess small effective mass ($\sim m_e$, cut 1), while the enclosed pockets exhibit very large effective mass (cut 2). The coexistence of light and heavy QPs is consistent with the results obtained from $(001)_p$-oriented films, confirming that this is an intrinsic property of the electronic structure of $CaRuO_3$. Detailed analysis shows that the effective mass for the heavy QP is $\sim 15 \pm 2m_e$ at 17 K, similar to the results obtained from $(001)_p$ oriented films. Note that the heavy QPs seen in $(001)_p$ and $(100)_p$ films are essentially the same band centered at $(k_x,k_y,k_z)=(\pm\pi/2,0,\pm\pi/2)$ (and symmetry-similar points, see Figs. 3(b) and S4(b)). This indicates that the observed heavy QP band is heavy along all three directions in momentum space (and therefore makes a large contribution to the electronic specific heat). This could not be reproduced by DFT calculations, where flat bands can be obtained only along some specific momentum direction (not along all momentum directions) (see Fig. S3). As the temperature increases, the heavy QP weight is quickly suppressed, while its effective mass, deduced from the band dispersion, shows a slight decrease to $12.5 \pm 2m_e$ at 140 K (bottom in Fig. S4(c)), which is barely above the uncertainty level due to the low QP intensity at this temperature. While a quantitative understanding of the effective mass with varying temperature requires further studies, the destruction of heavy QP at high temperature is in accordance with the DFT + DMFT calculations, which also predicts an increase of the mass enhancement factor $1/Z$ at low temperature for typical Hund's metal such as $CaRuO_3$ [10][11]. It is worth mentioning that the light QP bands show no temperature dependence and can be clearly observed even at the highest measurement temperature ($\sim$ 200 K).

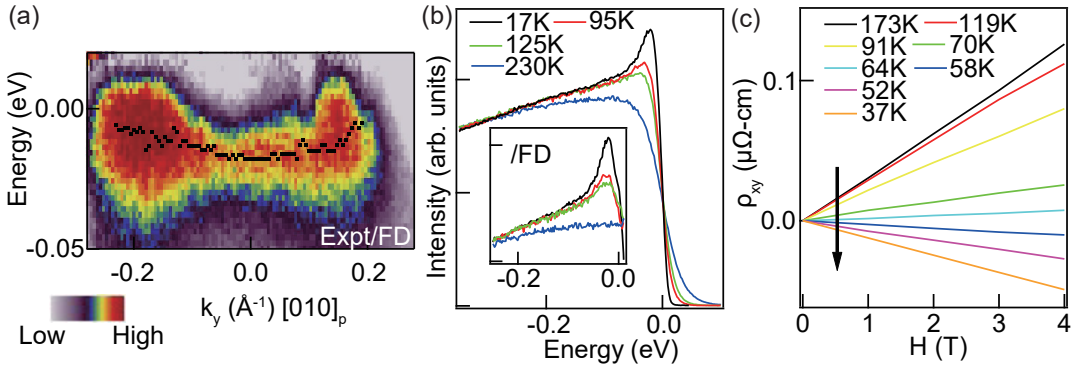

FIG. S 5. (a) shows the full spectral function near E_f for the heavy QP band for $(001)_p$ films, whose EDCs are fitted to yield the dispersion of the heavy QP band (black dots in Fig. 3(b)). The spectrum is obtained by dividing the experimental ARPES spectra in Fig. 3(b) in the manuscript by a convolution of Fermi-Dirac function and a Gaussian function, mimicking the thermal and instrumental broadening, respectively. (b) Temperature dependence of the heavy QP in $(001)_p$ films. The EDCs are taken at (k_y, k_z)=(0,-π/2), i.e., the white vertical cut in Fig. 3(b) of the manuscript. The inset is the APRES data divided by Fermi-Dirac function convoluted by a Gaussian function. This dataset is fitted to yield the results for $(001)_p$ films, as shown in Fig. 4(b) in the manuscript. (c) Hall resistivity vs magnetic field (its slope is Hall coefficient) as a function of temperature.

Since the heavy QP is right near the Fermi level, in order to accurately extract the heavy QP dispersion and effective mass, we divide the measured ARPES spectra by the Fermi-Dirac function convolted by a Gaussian function. The results of such an analysis for $(001)_p$ films is shown in Fig. S5(a). The results reveal that the heavy QP band is electron-like with a fitted effective mass $m^* = 13.5 \pm 1.5\ m_e$ (black dots). Figure S5(b) shows the temperature dependence of the EDC for a $(001)_p$ film, which shows a rapid destruction of QP upon warming up. Note that the observed change is not caused by a trivial thermal broadening effect, as the thermal broadening is already taken into account by the division of the Fermi-Dirac function (inset). The results from both Figs. S5(b) and 4(a) have been carefully checked by thermal cycling to eliminate the extrinsic effect from sample aging. Concomitant with the emergence of heavy electron-like QPs at low temperature, the Hall coefficient begins to show obvious change near 150 K and eventually crosses over from hole to electron carriers at $\sim$ 64 K, as shown in Fig. S5(c). We note that the detailed crossover temperature could be dependent on the sample quality, i.e., the QP spectral weight. For example, the crossover temperature from hole to electron carrier takes place at $\sim$ 50 K in [12], which is slightly lower than the crossover temperature in our samples. Nevertheless, the qualitative behavior and trend is similar, indicating that the connection between ARPES spectral weight and transport properties is intrinsic in $CaRuO_3$.

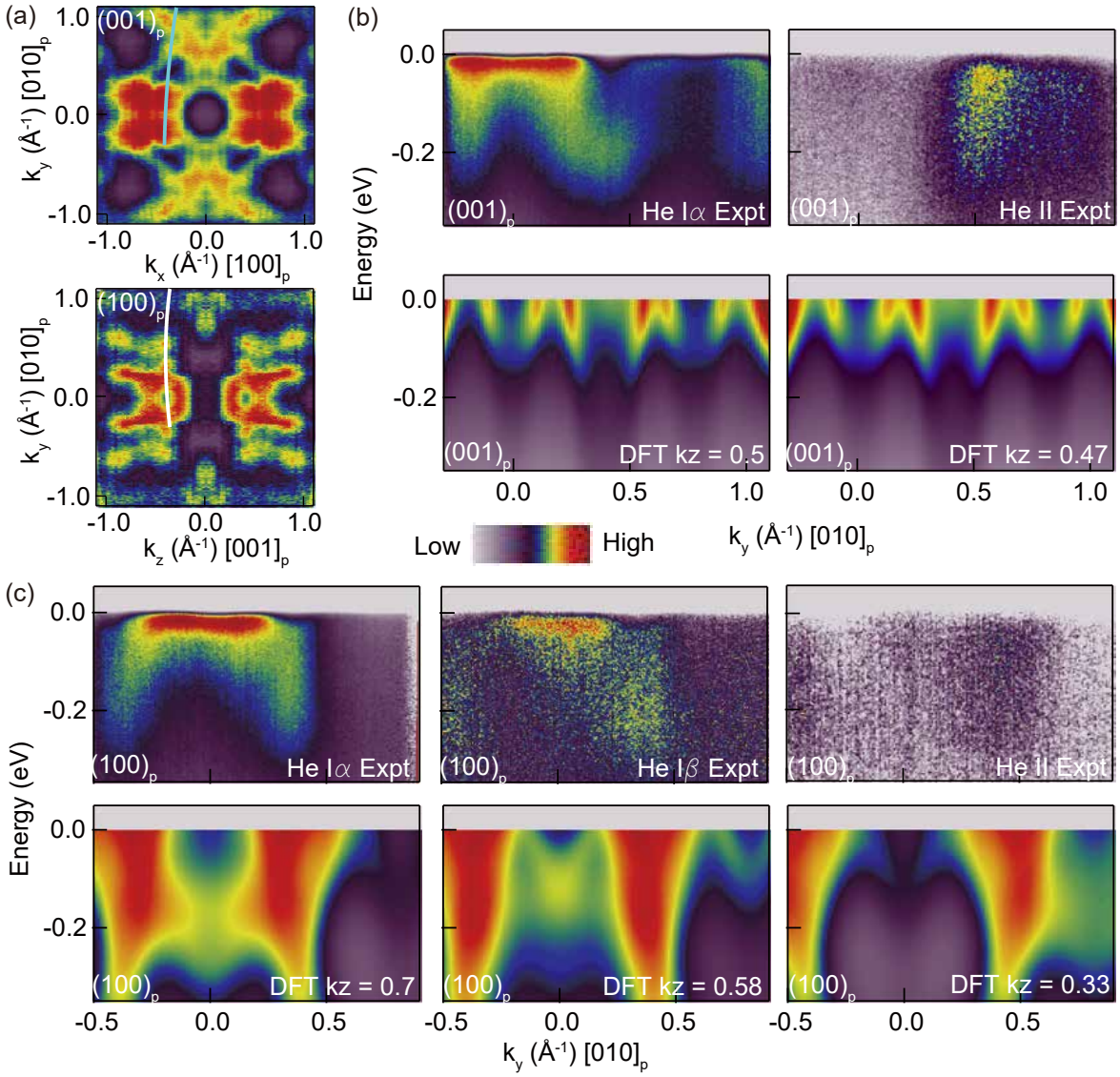

FIG. S 6. Photon energy dependence and comparison with DFT calculations for both $(001)_p$ and $(100)_p$ films. (a) Fermi surface for both $(001)_p$ and $(100)_p$ films taken with He Iα photons (21.2 eV), same as Fig. 2(b) and Fig. 2(e). The slanted cyan and white curves indicate the momentum cut position in (b) and (c), respectively. (b) the energy-momentum dispersion along the cyan curve in (a) for the $(001)_p$ film taken with He Iα and He II photons, in comparison with the DFT calculations at k_z cuts (in unit of π/a_0) corresponding to an inner potential of 14.4 eV. (c) the energy-momentum dispersion along the white curve in (a) for the $(100)_p$ film taken with He Iα, He Iβ and He II photons, in comparison with the DFT calculations at k_z cuts corresponding to an inner potential of 11 eV. The inner potential values are obtained from matching the He Iα Fermi surface map with DFT calculations (Fig. 2). The DFT simulations includes a k_z broadening of 0.1 π/a_0 (to take into account of limited escape depth of photoelectrons) and QP lifetime broadening (quadratic in energy expected for a FL), in a manner similar to Figs. S1 and S2.

In Fig. S6, we show ARPES data taken with He I α (21.2 eV), He Iβ (23.087 eV) and He II (40.8 eV) photons, to confirm the bulk nature of the observed QP bands and compare with DFT calculations. Due to the very low emisssion intensity from He Iβ and He II photons, the QP bands are not very well resolved and the data statistics are much poorer compared to He I α data. Fig. S6(b) shows the He Iα and He II data for a $(001)_p$ film, taken along the same momentum cut (shown as cyan curve in Fig. S6(a)), to compare with the DFT calculations. Using the inner pontetial of 14.4 eV, estimated by matching the He Iα Fermi surface map and DFT calculations (Fig. 2(b,c)), He II photons aproximately probe the k_z cut at 0.47 π/a_0, very close to the He Iα cut. While the light QP bands show somewhat similar dispersion for He Iα and He II photons, in agreement with DFT calculations, the heavy QP bands are much

weaker in the He II data. This implies that the k_z dispersion of heavy QP bands are not well captured by the DFT calculations, as discussed in the manuscript. Similar conclusions could be drawn for the $(100)_p$ film as shown in Fig. S6(c). Strong light QP bands can be seen near $k_y \sim 0.5\pi/a_0$, due to the strong band folding from oxygen octahedral rotation, which is in good agreement with DFT calculations. On the other hand, the heavy QP bands move upward with increasing photon energies and eventually disappear in He II data, confirming its bulk nature. Similar to the $(001)_p$ film, the heavy QP bands are not described well by DFT calculations.

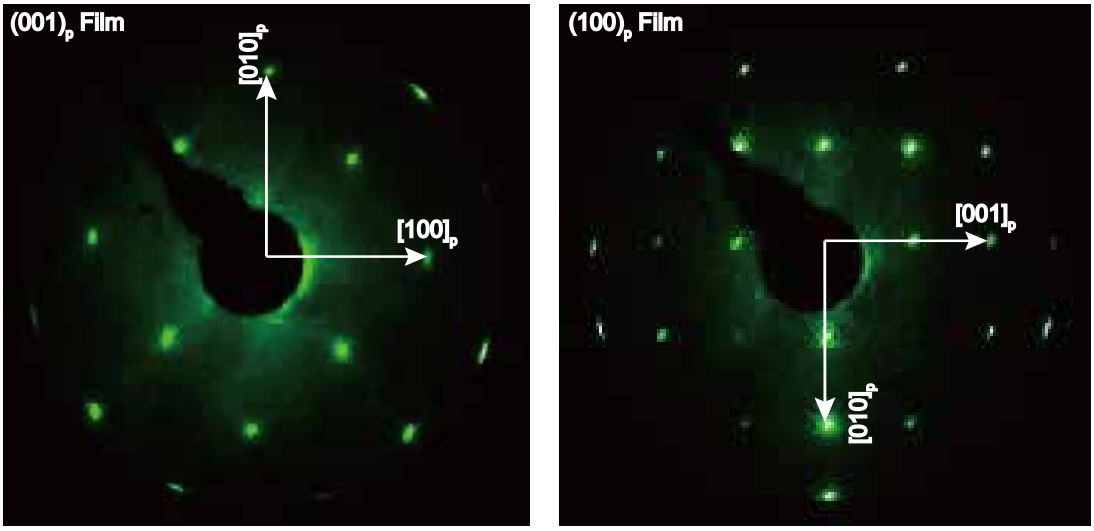

FIG. S 7. Enlarged LEED pattens for both $(001)_p$ (left) and $(100)_p$ (right) films. The white arrows indicate the in plane diffraction peaks corresponding to the pseudocubic lattice (without considering octahedral rotation). The LEED patterns are consistent with bulk-like octahedral rotations, without obvious sign of additional structural distortion at the surfaces.

* Yang Liu and Hari P. Nair contribute equallly to this work. Author to whom correspondence should be addressed: kmshen@cornell.edu

[1] T. Kiyama, K. Yoshimura, K. Kosuge, Y. Ikeda, and Y. Bando, Phys. Rev. B **54** R756 (1996).
[2] D. E. Shai, C. Adamo, D.W. Shen, C. M. Brooks, J.W. Harter, E. J. Monkman, B. Burganov, D. G. Schlom, and K. M. Shen, Phys. Rev. Lett. **110** 087004 (2013).
[3] M. Schneider, D. Geiger, S. Esser, U. S. Pracht, C. Stingl, Y. Tokiwa, V. Moshnyaga, I. Sheikin, J. Mravlje, M. Scheffler, and P. Gegenwart,, Phys. Rev. Lett. **112** 206403 (2014).
[4] G. Cao, O. Korneta, S. Chikara, L. E. DeLong, and P. Schlottmann, Solid State Commun. **148** 305 (2008).
[5] N. Kikugawa, L. Balicas, and A. P. Mackenzie, J. Phys. Soc. Jpn. **78** 014701 (2009).
[6] C. S. Alexander, S. McCall, P. Schlottmann, J. E. Crow, and G. Cao, Phys. Rev. B **72** 024415 (2005).
[7] A. P. Mackenzie, J. W. Reiner, A. W. Tyler, L. M. Galvin, S. R. Julian, M. R. Beasley, T. H. Geballe, and A. Kapitulnik, Phys. Rev. B **58** R13318 (1998).
[8] A. T. Zayak, X. Huang, J. B. Neaton, and Karin M. Rabe, Phys. Rev. B **74** 094104 (2006).
[9] H. T. Dang, J. Mravlje, A. Georges and A. J. Millis, Phys. Rev. Lett. **115** 107003 (2015).
[10] H. T. Dang, J. Mravlje, A. Georges and A. J. Millis, Phys. Rev. B **91** 195149 (2015).
[11] X. Deng, K. Haule, and G. Kotliar, Phys. Rev. Lett **116** 256401 (2016)
[12] S. C. Gausepohl, M. Lee, R. A. Rao, and C. B. Eom, Phys. Rev. B **54** 8996 (1996).